universe

IMPACT FACTOR 2.9

CITESCORE 3.6

Article

A Systematic Study of Two-Neutrino Double Electron Capture

Ovidiu Niţescu, Stefan Ghinescu, Sabin Stoica and Fedor Šimkovic

Special Issue

Recent Advances in Double Beta Decay Investigations: In Honor of Prof. Sabin Stoica at His 70th Anniversary

Edited by

Prof. Dr. Mihai Horoi, Prof. Dr. Hiro Ejiri and Dr. Andrei Neacsu

MDPI

https://doi.org/10.3390/universe10020098

universe

MDPI

Article

A Systematic Study of Two-Neutrino Double Electron Capture

Ovidiu Nițescu [1,2,3], Stefan Ghinescu [2,3,4], Sabin Stoica [2] and Fedor Šimkovic [1,5,*]

[1] Faculty of Mathematics, Physics and Informatics, Comenius University in Bratislava, 842 48 Bratislava, Slovakia; ovidiu.nitescu@fmph.uniba.sk
[2] International Centre for Advanced Training and Research in Physics, P.O. Box MG-12, RO-077125 Măgurele, Romania; stefan.ghinescu@nipne.ro (S.G.); sabin.stoica@cifra-c2unesco.ro (S.S.)
[3] "Horia Hulubei" National Institute of Physics and Nuclear Engineering, 30 Reactorului, P.O. Box MG-6, RO-077125 Măgurele, Romania
[4] Department of Physics, University of Bucharest, 405 Atomiştilor, P.O. Box MG-11, RO-077125 Măgurele, Romania
[5] Institute of Experimental and Applied Physics, Czech Technical University in Prague, 110 00 Prague, Czech Republic
* Correspondence: fedor.simkovic@fmph.uniba.sk

Abstract: In this paper, we update the phase-space factors for all two-neutrino double electron capture processes. The Dirac–Hartree–Fock–Slater self-consistent method is employed to describe the bound states of captured electrons, enabling a more realistic treatment of atomic screening and more precise binding energies of the captured electrons compared to previous investigations. Additionally, we consider all *s*-wave electrons available for capture, expanding beyond the K and L_1 orbitals considered in prior studies. For light atoms, the increase associated with additional captures compensates for the decrease in decay rate caused by the more precise atomic screening. However, for medium and heavy atoms, an increase in the decay rate, up to 10% for the heaviest atoms, is observed due to the combination of these two effects. In the systematic analysis, we also include capture fractions for the first few dominant partial captures. Our precise model enables a close examination of low Q-value double electron capture in ^{152}Gd, ^{164}Er, and ^{242}Cm, where partial KK captures are energetically forbidden. Finally, with the updated phase-space values, we recalculate the effective nuclear matrix elements and compare their spread with those associated with $2\nu\beta^-\beta^-$ decay.

Keywords: double beta decay; two-neutrino double electron capture; phase-space factor; effective nuclear matrix elements

Citation: Nițescu, O.; Ghinescu, S.; Stoica, S.; Šimkovic, F. A Systematic Study of Two-Neutrino Double Electron Capture. *Universe* **2024**, *10*, 98. https://doi.org/10.3390/universe10020098

Academic Editor: Francesco Terranova

Received: 11 January 2024
Revised: 14 February 2024
Accepted: 16 February 2024
Published: 17 February 2024

1. Introduction

Exploring second-order weak interaction nuclear transitions represents a crucial channel in addressing unresolved challenges within modern physics. The detection of neutrinoless double beta decay (DBD) holds particular significance, as it would confirm the Majorana nature of neutrinos [1] (meaning they are their own antiparticles), and potentially provide insights into the mechanism generating their mass, as well as into charge-parity (CP) violation in the lepton sector [2–8]. Moreover, it would mark the first instance of the detection of a lepton number-violating process in laboratory. These types of beyond the Standard Model (SM) processes might play a significant role in certain leptogenesis mechanisms, which may elucidate the prevalence of matter over antimatter in the Universe [9,10].

Currently, the most studied modes of DBD involve the emission of two electrons from neutron-rich candidate isotopes: the two-neutrino mode ($2\nu\beta^-\beta^-$) and the neutrinoless mode ($0\nu\beta^-\beta^-$). While the latter remains experimentally elusive [11–18], the former serves as a playground to test different hypotheses and the predictive strengths of the nuclear structure models [19–21], and to constrain various parameters associated with physics beyond the SM [22–32]. A comprehensive and recent review on the latter topic can be found in [33].

DBD of proton-rich isotopes is also possible and is currently in the early stages of experimental exploration [34]. There are three such DBD modes [35,36]: the double-positron emitting ($0\nu/2\nu\beta^+\beta^+$) mode, the single electron capture with coincident positron emission ($0\nu/2\nu\mathrm{EC}\beta^+$) mode, and the double electron capture ($0\nu/2\nu$ECEC) mode. Experimental measurements of these modes have received less attention due to their longer half-lives compared to the $2\nu\beta^-\beta^-$ decay mode, mostly due to their lower Q-values. However, their distinct signatures might help in their detection, especially if coincidence trigger logic can be employed [34]. There are some positive indications of the 2νECEC mode for ^{130}Ba and ^{132}Ba from geochemical measurements [37–39] and for ^{78}Kr [40,41]. Recently, the XENON1T collaboration reported the direct observation of the 2νECEC mode in ^{124}Xe [42,43].

From the theoretical point of view, the pioneer estimates of the decay rates for 2νECEC have been obtained by Primakoff and Rosen [44,45], followed up by the ones made by Vergados [46] and by Kim and Kubodera [47]. In these early stages, the predictions were based on a non-relativistic treatment for the captured electrons. Doi and Kotani were the first to present a detailed theoretical formulation for the process and to include the relativistic effects [35]. Still, the calculations are based on the atomic structure of a point-like nucleus, for which the electron bound states are known analytically. At the same time, Boehm and Vogel presented the results for some selected 2νECEC cases, but not many details of the calculations are provided [48]. Recently, the treatment of the atomic screening was improved using a Thomas–Fermi model for an atomic cloud [49–51]. The diffuse nuclear surface effects have also been accounted for through a realistic charge distribution inside the nucleus [50,51].

Although 2νECEC, by its very nature, stands at the interface between nuclear and atomic physics, some aspects regarding the atomic structure calculations have been overlooked or treated simplistically in previous investigations. In this paper, we employ the Dirac–Hartree–Fock–Slater (DHFS) self-consistent framework, providing an enhanced description of atomic screening for the systems involved in the decay and a more rigorous estimation of the binding energies for the captured electrons. We mention that the DHFS atomic potential includes the finite nuclear size and diffuse nuclear surface effects. Furthermore, we extend our analysis to include all s-wave electrons available for capture, surpassing the K and L_1 orbitals considered in prior studies.

We demonstrate that, for light atoms undergoing the 2νECEC process, the decrease in the decay rate resulting from more realistic screening is balanced out by the increase associated with opening the capture from higher orbitals than K and L_1. However, this balance is not observed for medium and heavy atoms, where the latter improvement in our model leads to a considerable increase in the decay rate, up to 10% for the heaviest atoms. For all cases undergoing 2νECEC, we provide the capture fractions for the first few dominant channels. We specifically address the low Q-value 2νECEC transitions of ^{152}Gd, ^{164}Er, and ^{242}Cm, for which the capture of both K shell electrons is energetically forbidden. Finally, with the updated phase-space values, we reexamine the effective nuclear matrix elements and compare their spread with those associated with $2\nu\beta^-\beta^-$.

2. Formalism for the Two-Neutrino Double Electron Capture

2.1. Energetics

We investigate the two neutrino double electron capture (2νECEC) process,

$$2e^- + (A, Z+2) \rightarrow (A, Z) + 2\nu_e, \tag{1}$$

in which the initial nucleus $(A, Z+2)$ captures two atomic electrons, changing its atomic number by two units and emitting two neutrinos. If the electrons are captured from x and y atomic orbitals, we denote the process as 2νxy. To keep the notation simple, we use the X-ray notation for the orbitals, i.e., x and y $= K, L_1, M_1, N_1, \ldots$ Following the 2νxy process, the final atomic system, while electrically neutral, remains in an excited atomic state, with vacancies in the orbitals x and y from which the electrons were initially captured. Consequently, the 2νECEC process is followed by atomic de-excitation, involving

a sequence of X-ray emissions and Auger electrons released from the outer shells. Figure 1 provides a schematic illustration of two channels of the 2νECEC process in ^{124}Xe. The top panel shows that both electrons are captured from the K orbital ($2\nu KK$), while the bottom panel shows that they are captured from L_1 orbital ($2\nu L_1 L_1$). It is worth noting that the atomic de-excitation results in different energy deposition in the detector depending on whether the capture is from the K or L_1 shells. This is due to the fact that the atomic relaxation following $L_1 L_1$ capture emits less energy compared to the KK capture.

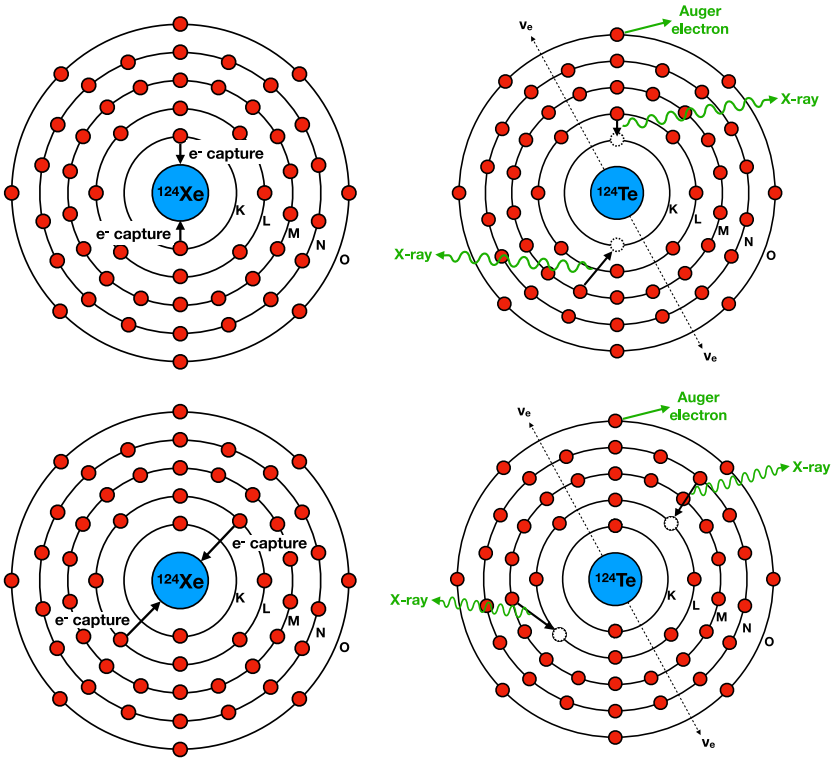

Figure 1. A simplified schematic representation of the 2νECEC process in ^{124}Xe. Top panels: both electrons are captured from K shell. Bottom panels: both electrons are captured from L shell. Left panels: two bound electrons from K (top) or L (bottom) shell are captured by the initial nucleus ^{124}Xe. Right panels: the atomic relaxation of the final neutral atomic system ^{124}Te, with two holes in K (top) or L (bottom) shell. The de-excitation is performed via X-ray emissions and Auger electrons from outer shells. The figure is reproduced from [52] by adding the schematic representation of the $2\nu L_1 L_1$ process in ^{124}Xe.

We adopt the following energy balance,

$$\mathcal{M}_{\rm gs}(A, Z+2) - \mathcal{M}_{\rm gs}(A, Z) = \omega_{\rm x} + \omega_{\rm y} + \mathcal{M}_{\rm xy}(A, Z) - \mathcal{M}_{\rm gs}(A, Z), \tag{2}$$

which indicates that the difference in the atomic masses of the initial and final systems in ground states, usually denoted as $Q = \mathcal{M}_{\rm gs}(A, Z+2) - \mathcal{M}_{\rm gs}(A, Z)$, is shared between neutrinos with energies $\omega_{\rm x}$ and $\omega_{\rm y}$, and the atomic relaxation of the final atom. The mass $\mathcal{M}_{\rm xy}(A, Z)$ corresponds to an atomic excited state of the final neutral system, with holes in the shell x and y from where the electrons were captured in the initial atom, and it can be written as

$$\mathcal{M}_{\rm xy}(A, Z) = E_f + Z m_e - B_{\rm xy}(Z) \tag{3}$$

where E_f is the nuclear mass (energy) of the final nucleus, Zm_e is the rest energy of the final atomic cloud (m_e is the mass of the electron), and $B_{\rm xy}(Z)$ is the total electron binding energy of the final system with a configuration with two holes. We adopt the units in which $\hbar = c = 1$. One can see that the atomic relaxation energy can be written as a difference in the total electron binding energies of the final atom with gs and xy configurations,

$$R_{xy} = B_{gs}(Z) - B_{xy}(Z). \tag{4}$$

The total energy of the emitted neutrinos can be written as

$$\omega_x + \omega_y = Q - R_{xy} \tag{5}$$

and, making the usual approximation that $B_{xy}(Z) - B_{gs}(Z+2) = -|t_x| - |t_y|$, we finally obtain [35,49,51]

$$\begin{aligned} \omega_x + \omega_y &= E_i - E_f + 2m_e - |t_x| - |t_y| \\ &= E_i - E_f + e_x + e_y, \end{aligned} \tag{6}$$

where t_x and $e_x = m_e - |t_x|$ are, respectively, the binding and the total energy for the electrons in shell x.

2.2. Half-Life

Following the separation of the decay rate from [35,49], the inverse half-life of the 2νECEC process from 0^+ ground state of the initial nucleus to the 0^+ ground state of the final nucleus is given by

$$\left[T_{1/2}^{2\nu\mathrm{ECEC}}\right]^{-1} = g_A^4 \left| M^{2\nu\mathrm{ECEC}} \right|^2 G_{K\to\mathrm{edge}}^{2\nu\mathrm{ECEC}}, \tag{7}$$

where g_A is the axial coupling constant, $G_{K\to\mathrm{edge}}^{2\nu\mathrm{ECEC}}$ is the phase-space factor (PSF) discussed later, and $M^{2\nu\mathrm{ECEC}}$, the nuclear matrix element (NME), is given by

$$M^{2\nu\mathrm{ECEC}} = -\frac{m_e}{\tilde{A}} \left[M_{\mathrm{GT}}^{2\nu\mathrm{ECEC}} - \left(\frac{g_V}{g_A}\right)^2 M_{\mathrm{F}}^{2\nu\mathrm{ECEC}} \right]. \tag{8}$$

Here, $\tilde{A} = 1.12A^{1/2}$ in MeV and g_V is the vector coupling constant. This choice of $\tilde{A}$ reproduces the average excitation energies in the intermediate nucleus for a wide range of isotopes [53]. Nevertheless, there are reasons supporting the use of a single value for both, as discussed in [53]. The double Gamow–Teller (GT) and Fermi (F) transition matrix elements, in closure approximation, are $M_{\mathrm{GT}}^{2\nu\mathrm{ECEC}} = \langle 0_f^+ \left| \sum_{j,k} \tau_j^- \tau_k^- \boldsymbol{\sigma}_j \boldsymbol{\sigma}_k \right| 0_i^+ \rangle$ and $M_{\mathrm{F}}^{2\nu\mathrm{ECEC}} = \langle 0_f^+ \left| \sum_{j,k} \tau_j^- \tau_k^- \right| 0_i^+ \rangle$ [49]. Here, $\tau_{j,k}^-$ is the isospin-lowering operator, transforming a proton into a neutron and $\boldsymbol{\sigma}_{j,k}$ is the nucleon spin operator.

It is important to highlight that the factorization of the half-life in Equation (7) assumes the closure approximation [35]. Consequently, the PSFs outlined below should be paired with NMEs computed within the same approximation. However, there have been various studies computing NMEs beyond the closure approximation and overlooking the constraint above [54–56]. Despite the lack of consistency, the predictions for half-lives are notably close to experimental values. In this study, we adhere to the closure approximation for comparison purposes. It is worth mentioning that an alternative factorization of the 2νECEC half-life, beyond the closure approximation, will be presented elsewhere.

In this paper, we consider that captures can occur from any occupied $s_{1/2}$ orbitals of the initial atom, i.e., $K, L_1, M_1, \ldots$ The capture from other orbitals is suppressed, firstly because the higher orbital angular momentum of these orbitals reduces the capture probability, and secondly, smaller NMEs are associated with these captures [35]. Under these assumptions, we found that the PSF expression is

$$G^{2\nu\mathrm{ECEC}}_{K\to\mathrm{edge}} = \frac{m_e(G_F|V_{ud}|m_e^2)^4}{16\pi^3}\frac{2\tilde{A}}{3m_e^2}\frac{1}{m_e^3}\sum_{\substack{\mathrm{x,y}=K \\ E_I-E_F+e_\mathrm{x}+e_\mathrm{y}>0}}^{\mathrm{edge}} \mathcal{B}^2_\mathrm{x}\mathcal{B}^2_\mathrm{y} \times \int_0^{E_I-E_F+e_\mathrm{x}+e_\mathrm{y}} \Big[\langle K_{n,\mathrm{xy}}\rangle^2 + \langle L_{n,\mathrm{xy}}\rangle^2 + \langle K_{n,\mathrm{xy}}\rangle\langle L_{n,\mathrm{xy}}\rangle\Big]\omega_\mathrm{x}^2\omega_\mathrm{y}^2 d\omega_\mathrm{x} = \sum_{\substack{\mathrm{x,y}=K \\ E_I-E_F+e_\mathrm{x}+e_\mathrm{y}>0}}^{\mathrm{edge}} G^{2\nu\mathrm{xy}}. \quad (9)$$

where G_F is the Fermi coupling constant and V_{ud} the first element of the Cabibbo–Kobayashi–Maskawa (CKM) matrix. The sums are running over all occupied orbitals of the initial atomic system from where the electrons can be captured. The "edge" label refers to the last such orbital. The localization probability for an electron from shell x on the nuclear surface can be written as [35,49],

$$\mathcal{B}^2_\mathrm{x} = \frac{1}{4\pi m_e^3}\Big[g^2_\mathrm{x}(R) + f^2_\mathrm{x}(R)\Big], \quad (10)$$

in terms of the large- and small-component radial wave functions describing the bound state, $g_\mathrm{x}(r)$ and $f_\mathrm{x}(r)$, respectively, evaluated on the nuclear surface $R = 1.2A^{1/3}$. The factors $\langle K_{n,\mathrm{xy}}\rangle$ and $\langle L_{n,\mathrm{xy}}\rangle$ can be written as

$$\begin{aligned}\langle K_{n,\mathrm{xy}}\rangle &= \frac{1}{-e_\mathrm{x}+\omega_\mathrm{x}+\langle E_n\rangle - E_i} + \frac{1}{-e_\mathrm{y}+\omega_\mathrm{y}+\langle E_n\rangle - E_i} \\ \langle L_{n,\mathrm{xy}}\rangle &= \frac{1}{-e_\mathrm{x}+\omega_\mathrm{y}+\langle E_n\rangle - E_i} + \frac{1}{-e_\mathrm{y}+\omega_\mathrm{x}+\langle E_n\rangle - E_i}\end{aligned} \quad (11)$$

where $\langle E_n\rangle$ is a suitably chosen excitation energy for the intermediate nucleus, $(A, Z+1)$. In the actual calculations, the energy difference $\langle E_n\rangle - E_i = \tilde{A} - Q/2 + m_e$.

For comparison with the results of the previous investigations, we define also the PSF for captures from K and L_1 orbitals only,

$$G^{2\nu\mathrm{ECEC}}_{K\to L_1} = G^{2\nu KK} + 2G^{2\nu KL_1} + G^{2\nu L_1L_1} \quad (12)$$

which is a particularization of Equation (9). The factor of 2 stems from the equal contributions of 2νxy and 2νyx captures in the total decay rate for any x $\neq$ y orbitals.

2.3. Electron Bound States Description

Accurate computation of the PSFs for any 2νECEC process requires precise atomic structure calculations for the atomic systems involved in the process. For this purpose, we employed the Dirac–Hartree–Fock–Slater (DHFS) self-consistent framework. The nuclear, electronic, and exchange components of the DHFS potential, as well as the convergence of the self-consistent method, were described in detail in [57,58], based on the RADIAL subroutine package [59], which we also used in our calculations. In a relativistic framework and for a spherically symmetric potential of the atomic systems, the large- and small-component radial wave functions from Equation (10) obey the following system of coupled differential equations

$$\begin{aligned}\left(\frac{d}{dr} + \frac{\kappa+1}{r}\right)g_{n\kappa}(r) - (e_{n\kappa} - V_\mathrm{DHFS}(r) + m_e)f_{n\kappa}(r) = 0, \\ \left(\frac{d}{dr} - \frac{\kappa-1}{r}\right)f_{n\kappa}(r) + (e_{n\kappa} - V_\mathrm{DHFS}(r) - m_e)g_{n\kappa}(r) = 0.\end{aligned} \quad (13)$$

In previous sections, the shells referred to as x or y can be uniquely identified by the state $n\kappa$, where n represents the principal quantum number and κ corresponds to the relativistic quantum number.

In Table 1, we present a comparison between experimental binding energies and values predicted by different models for the selected isotopes (Kr, Xe, and Ba) undergoing the 2νECEC process. The model proposed by [35], assuming a uniform charge distribution for the nucleus with no screening due to the atomic charge, fails to reproduce the experimental data. Models incorporating atomic screening and diffuse nuclear surface effects, as seen in [50,51], using a Thomas–Fermi screening function and a realistic proton density inside the nucleus, respectively, provide improved results but still yield binding energies significantly larger than the experimental ones. Notably, the DHFS self-consistent method employed in this work successfully reproduces experimental binding energies within a 1% margin.

Table 1. The binding energies, t_x, in units of eV, for all occupied $s_{1/2}$ orbitals of the neutral atoms, Kr, Xe and Ba, undergoing 2νECEC process. The experimental data are sourced from [60], our values are obtained with the DHFS self-consistent method, and values from prior studies are taken from [35] and [50,51].

Shell $(n\ell_j)$	t_x **[35] (eV)**	t_x **[50,51] (eV)**	t_x **[This Work] (eV)**	t_x **[Experiment] [60] (eV)**
		Kr		
$K(1s_{1/2})$	$-17,936$	$-17,700$	$-14,280$	$-14,327 \pm 2$
$L_1(2s_{1/2})$	-4507	-3100	-1902	-1927 ± 2
$M_1(3s_{1/2})$	–	–	-278	-292 ± 2
$N_1(4s_{1/2})$	–	–	-27.46	-27.51 ± 0.1
		Xe		
$K(1s_{1/2})$	$-41,340$	$-39,400$	$-34,556$	$-34,565 \pm 2$
$L_1(2s_{1/2})$	$-10,424$	-7800	-5417	-5452 ± 2
$M_1(3s_{1/2})$	–	–	-1122	-1149 ± 2
$N_1(4s_{1/2})$	–	–	-208	-213 ± 2
$O_1(5s_{1/2})$	–	–	-23.63	-23.40 ± 0.1
		Ba		
$K(1s_{1/2})$	$-44,610$	$-42,400$	$-37,450$	$-37,442 \pm 2$
$L_1(2s_{1/2})$	$-11,293$	-8500	-5961	-5991 ± 2
$M_1(3s_{1/2})$	–	–	-1274	-1293 ± 2
$N_1(4s_{1/2})$	–	–	-256	-254 ± 2
$O_1(5s_{1/2})$	–	–	-38	-31 ± 2
$P_1(6s_{1/2})$	–	–	-4.64	-5.21 ± 0.1

3. Results and Discussions

The PSFs for captures from K and L_1 shells only, $G^{2\nu\mathrm{ECEC}}_{K\to L_1}$, calculated for the 2νECEC cases previously investigated, are shown in Table 2. Here, we have assumed the same Q-values as in [49]. Our results are consistently lower by about 5% than the values reported in [49], with a couple of exceptions observed in ^{92}Mo and ^{180}W. Our results generally fall within 70% of the values reported in [50,51], with a noticeable dependency on A: for low mass numbers, our PSFs are lower than those in [50,51], but as the mass number increases, the factors in this work approach and even exceed the values reported in that reference, suggesting a discrepancy in the underlying models. In contrast, the $G^{2\nu\mathrm{ECEC}}_{K\to L_1}$ values derived in this work exhibit a consistent 10–20% reduction compared to the ones provided in [35], which could be attributed to the fact that, in [35], the screening effect is not accounted for. We chose not to display the $G^{2\nu\mathrm{ECEC}}_{K\to L_1}$ values from [48], since it does not employ the same definition of the PSF due to a different separation of the decay rate.

In Table 3, we present the total PSFs $G^{2\nu\mathrm{ECEC}}_{K\to\mathrm{edge}}$, as well as the capture fractions for selected shell pairs, for all nuclei for which 2νECEC is energetically possible, and EC

is energetically forbidden. When comparing with one of the most precise calculations available [49] (column four of Table 2), one can see the following trend. For light atoms, the more rigorous treatment of atomic screening balances out the effect of accounting for all $\kappa = -1$ shells. The only exception is ^{40}Ca, where the PSF value computed using all $\kappa = -1$ shells is higher by about 7.5% than the one in [49]. The difference is induced by the interplay between the binding energies and Q-value in the PSF integral (see Equation (9)). For medium and heavy atoms, there is an increase in the decay rate compared to results from [49], almost linear in Z, reaching about 10% for the heaviest atoms.

The low Q-value transitions of ^{152}Gd, ^{164}Er and ^{242}Cm exhibit an interesting behavior. In these cases, both the KK and the KL_1 captures are energetically forbidden, and the highest contribution to the total PSF is given by the L_1L_1, M_1M_1 and L_1M_1 captures. The values of the PSFs and capture fractions for these low Q-value transitions are given in Table 4.

Table 2. Comparison of the $G^{2\nu\mathrm{ECEC}}_{K\to L_1}$ (in units of 10^{-24} yr^{-1}) values from [35,49–51], with values obtained through the method explained in this study. The Q-values cited in [49] were utilized. In cases where these values were not available, the Q was calculated using atomic masses provided in [61].

Nucleus	Q (MeV)	$G^{2\nu\mathrm{ECEC}}_{K\to L_1}$ [35] $(10^{-24}\mathrm{yr}^{-1})$	$G^{2\nu\mathrm{ECEC}}_{K\to L_1}$ [49] $(10^{-24}\mathrm{yr}^{-1})$	$G^{2\nu\mathrm{ECEC}}_{K\to L_1}$ [50,51] $(10^{-24}\mathrm{yr}^{-1})$	$G^{2\nu\mathrm{ECEC}}_{K\to L_1}$ [This Work] $(10^{-24}\mathrm{yr}^{-1})$
^{36}Ar	0.43259	–	–	2.900×10^{-4}	4.168×10^{-4}
^{40}Ca	0.19351	–	1.250×10^{-5}	1.020×10^{-5}	1.314×10^{-5}
^{50}Cr	1.1688	–	4.220×10^{-1}	2.380×10^{-1}	4.161×10^{-1}
^{54}Fe	0.6798	–	4.690×10^{-2}	3.021×10^{-2}	4.553×10^{-2}
^{58}Ni	1.9263	17.00	15.30	9.900	14.79
^{64}Zn	1.0948	–	1.410	1.030	1.364
^{74}Se	1.209169	–	5.656	3.410	5.454
^{78}Kr	2.8463	774.0	660.0	410.0	637.0
^{84}Sr	1.79	–	93.60	64.62	90.58
^{92}Mo	1.651	–	208.0	82.32	128.2
^{96}Ru	2.71451	2.740×10^{3}	2.400×10^{3}	1.450×10^{3}	2.328×10^{3}
^{102}Pd	1.1727	–	46.00	42.09	44.64
^{106}Cd	2.77539	6.220×10^{3}	5.410×10^{3}	4.299×10^{3}	5.269×10^{3}
^{108}Cd	0.27204	–	2.070×10^{-2}	6.820×10^{-2}	1.975×10^{-2}
^{112}Sn	1.91982	–	1.150×10^{3}	869.7	1.120×10^{3}
^{120}Te	1.71481	–	888.0	840.3	866.3
^{124}Xe	2.8654	2.020×10^{4}	1.720×10^{4}	1.510×10^{4}	1.685×10^{4}
^{126}Xe	0.92	–	46.10	60.59	44.98
^{130}Ba	2.619	1.630×10^{4}	1.500×10^{4}	1.477×10^{4}	1.464×10^{4}
^{132}Ba	0.844	–	39.10	61.98	38.12
^{136}Ce	2.37853	1.580×10^{4}	1.250×10^{4}	1.222×10^{4}	1.224×10^{4}
^{138}Ce	0.698	–	18.40	34.47	17.92
^{144}Sm	1.78259	–	5.150×10^{3}	6.436×10^{3}	5.055×10^{3}
^{152}Gd	0.0557	–	–	1.120×10^{-2}	5.989×10^{-7}
^{156}Dy	2.012	–	1.760×10^{4}	2.208×10^{4}	1.734×10^{4}
^{158}Dy	0.284	–	1.830×10^{-1}	3.191	1.751×10^{-1}
^{162}Er	1.844	1.810×10^{4}	1.500×10^{4}	2.008×10^{4}	1.470×10^{4}
^{164}Er	0.02507	–	–	8.300×10^{-3}	7.392×10^{-11}
^{168}Yb	1.40927	–	4.710×10^{3}	7.872×10^{3}	4.647×10^{3}
^{174}Hf	1.0988	–	1.580×10^{3}	3.432×10^{3}	1.563×10^{3}
^{180}W	0.1432	–	1.560×10^{-3}	1.478	1.321×10^{-3}
^{184}Os	1.453	–	1.290×10^{4}	2.422×10^{4}	1.275×10^{4}
^{190}Pt	1.384	–	1.290×10^{4}	2.815×10^{4}	1.285×10^{4}
^{196}Hg	0.82	–	821.0	3.587×10^{3}	815.8

Table 3. Values of the $G^{2\nu\mathrm{ECEC}}_{K\to\mathrm{edge}}$ (in units of 10^{-24} yr^{-1}) and of the capture fractions for various shell pairs. The Q-values are computed using atomic masses provided in [61].

Nucleus	Q (MeV)	$G^{2\nu\mathrm{ECEC}}_{K\to\mathrm{edge}}$ $(10^{-24}\mathrm{yr}^{-1})$	KK (%)	KL_1 (%)	KM_1 (%)	KN_1 (%)	L_1L_1 (%)
^{36}Ar	0.4326	4.244×10^{-4}	83.40	14.23	1.62	–	0.61
^{40}Ca	0.1935	1.347×10^{-5}	81.38	15.44	2.07	0.16	0.73
^{50}Cr	1.1705	4.301×10^{-1}	81.35	15.39	2.18	0.12	0.73
^{54}Fe	0.68076	4.717×10^{-2}	80.41	16.01	2.35	0.16	0.80
^{58}Ni	1.9264	15.22	80.45	15.97	2.37	0.15	0.79
^{64}Zn	1.09502	1.407	79.73	16.50	2.48	0.14	0.85
^{74}Se	1.20924	5.648	78.64	17.03	2.74	0.30	0.92
^{78}Kr	2.84767	661.9	78.64	16.92	2.81	0.35	0.91
^{84}Sr	1.78977	94.16	77.83	17.33	2.98	0.44	0.96
^{92}Mo	1.65044	133.8	76.69	17.89	3.25	0.56	1.04
^{96}Ru	2.7145	2.437×10^{3}	76.64	17.85	3.31	0.60	1.04
^{102}Pd	1.20347	53.70	75.16	18.77	3.59	0.68	1.17
^{106}Cd	2.77539	5.540×10^{3}	75.71	18.31	3.55	0.69	1.11
^{108}Cd	0.27179	2.122×10^{-2}	65.39	24.87	5.12	1.01	2.26
^{112}Sn	1.91981	1.181×10^{3}	74.78	18.82	3.72	0.76	1.18
^{120}Te	1.73558	975.8	74.06	19.20	3.87	0.83	1.24
^{124}Xe	2.85674	1.756×10^{4}	74.22	19.00	3.88	0.86	1.22
^{126}Xe	0.91778	47.36	71.66	20.62	4.28	0.95	1.48
^{130}Ba	2.6237	1.570×10^{4}	73.57	19.31	4.00	0.92	1.27
^{132}Ba	0.84407	40.87	70.45	21.26	4.50	1.03	1.59
^{136}Ce	2.37853	1.303×10^{4}	72.88	19.67	4.14	0.97	1.33
^{138}Ce	0.69594	19.03	68.37	22.43	4.86	1.14	1.82
^{144}Sm	1.7824	5.417×10^{3}	71.11	20.67	4.49	1.07	1.50
^{150}Gd	1.28728	1.301×10^{3}	69.29	21.72	4.81	1.16	1.69
^{152}Gd	0.05567	1.547×10^{-6}	–	–	7.40×10^{-4}	1.04×10^{-3}	38.56
^{154}Dy	3.31234	2.490×10^{5}	71.29	20.48	4.51	1.09	1.47
^{156}Dy	2.00595	1.837×10^{4}	70.19	21.14	4.69	1.14	1.59
^{158}Dy	0.28282	2.028×10^{-1}	42.31	35.46	9.04	2.26	6.01
^{162}Er	1.84696	1.601×10^{4}	69.29	21.64	4.87	1.19	1.68
^{164}Er	0.02508	8.606×10^{-9}	–	–	–	–	0.87
^{168}Yb	1.40936	5.052×10^{3}	67.42	22.71	5.20	1.27	1.90
^{174}Hf	1.09994	1.724×10^{3}	64.94	24.06	5.62	1.39	2.20
^{180}W	0.14323	2.522×10^{-3}	5.94×10^{-5}	17.72	8.08	2.34	34.73
^{184}Os	1.45289	1.399×10^{4}	65.02	23.90	5.64	1.43	2.17
^{190}Pt	1.40132	1.519×10^{4}	63.83	24.50	5.84	1.50	2.32
^{196}Hg	0.81859	916.2	56.49	28.25	7.04	1.84	3.38
^{212}Rn	1.71019	1.400×10^{5}	61.36	25.58	6.27	1.68	2.63
^{214}Rn	0.15031	1.376×10^{-2}	–	1.07	1.38	0.52	39.52
^{218}Ra	1.42814	6.758×10^{4}	58.58	26.92	6.72	1.83	3.03
^{224}Th	1.16975	2.802×10^{4}	54.68	28.74	7.34	2.03	3.64
^{230}U	0.75251	2.393×10^{3}	42.80	33.66	9.16	2.59	5.87
^{236}Pu	0.45693	95.16	16.51	39.25	12.33	3.64	13.66
^{242}Cm	0.08682	1.243×10^{-3}	–	–	–	–	9.66
^{252}Fm	0.782	8.121×10^{3}	34.11	36.07	10.34	3.05	7.96
^{258}No	1.051	7.188×10^{4}	41.77	33.61	9.28	2.73	6.14

The inverse of the PSF is proportional to the half-life for each transition (see Equation (7)). This quantity is plotted in Figure 2 for all nuclei shown in Table 3 versus atomic number. One can see a decrease in the Q-value as the atomic number increases.

Finally, we investigate the effective matrix elements for the 2νECEC process of ^{78}Kr, ^{124}Xe, ^{130}Ba and ^{132}Ba. These can be obtained as

$$\left|M_{\text{eff}}^{2\nu\text{ECEC}}\right| = \frac{1}{\sqrt{T_{1/2}^{2\nu\text{ECEC}} G_{K\to\text{edge}}^{2\nu\text{ECEC}}}} = \frac{m_e}{\tilde{A}}\left|g_A^2 M_{\text{GT}}^{2\nu\text{ECEC}} - g_V^2 M_{\text{F}}^{2\nu\text{ECEC}}\right|. \quad (14)$$

using the experimental half-lives and the PSFs from Table 3. The effective NME values are presented in Table 5. It should be noted that, in the case of ^{132}Ba, there is also an experimental half-life measurement [38]. The authors state that the obtained value is tentative, and indeed, we obtain an effective NME value that is more than one order of magnitude larger than the others. Hence, we employ the half-life limit from [37]. Future measurements might clarify the situation, but we note that, in general, geochemical measurements tend to underestimate the half-lives, leading to overestimated effective NMEs. This may be a consequence of the difficulty in identifying the relevant production channel of the final atom [34]. Another interesting hypothesis is the variation in the weak interaction constant with time [62–64].

In Figure 3, we compare the values from Table 5 with the corresponding $2\nu\beta^-\beta^-$ effective nuclear matrix elements. These are defined similarly to the ECEC effective NMEs, but replacing isospin-lowering with isospin-rising operators in the definition of the Gamow–Teller and Fermi matrix elements. We note that effective matrix elements from both processes span similar ranges.

Table 4. Values of the $G_{K\to\text{edge}}^{2\nu\text{ECEC}}$ (in units of 10^{-24} yr^{-1}) and of the capture fractions for the dominant shell pairs in case of low Q-value transitions. The Q-values are computed using atomic masses provided in [61].

Nucleus	Q (MeV)	$G_{K\to\text{edge}}^{2\nu\text{ECEC}}$ (10^{-24}yr^{-1})	L_1L_1 (%)	L_1M_1 (%)	L_1N_1 (%)	L_1O_1 (%)	M_1M_1 (%)	M_1N_1 (%)	M_1O_1 (%)	N_1N_1 (%)	N_1O_1 (%)
^{152}Gd	0.05567	1.547×10^{-6}	38.56	35.94	10.12	1.84	7.56	4.17	0.75	0.57	0.21
^{164}Er	0.02508	8.606×10^{-9}	0.87	26.59	12.06	2.33	28.11	20.49	3.79	3.62	1.33
^{242}Cm	0.08682	1.243×10^{-3}	9.66	33.49	13.91	4.16	16.55	12.49	3.65	2.32	1.35

Table 5. Values or limits of the experimental half-life $M_{\text{eff}}^{2\nu\text{ECEC}}$. The Q-values are computed using atomic masses provided in [61]. The bottom row corresponds to the $2\nu\beta^-\beta^-$ decay of ^{134}Xe. For this case, the value of the effective NME was obtained from the lower half-life limit, and the PSF computed following [65] (0.225×10^{-22} yr^{-1} using $Q = 0.8258$ MeV).

Nucleus	$T_{1/2}^{2\nu\text{ECEC}}$ (yr)	$\left\|M_{\text{eff}}^{2\nu\text{ECEC}}\right\|$
^{78}Kr	$9.2^{+5.7}_{-2.9} \times 10^{21}$ [40]	$0.457^{+0.095}_{-0.098}$
	$1.9^{+1.3}_{-0.8} \times 10^{22}$ [41]	$0.318^{+0.100}_{-0.073}$
^{124}Xe	$(1.1 \pm 0.2) \times 10^{22}$ [43]	$0.072^{+0.008}_{-0.006}$
^{130}Ba	$(2.2 \pm 0.5) \times 10^{21}$ [38]	$0.170^{+0.023}_{-0.017}$
	$(6.0 \pm 1.1) \times 10^{20}$ [39]	$0.326^{+0.035}_{-0.026}$
^{132}Ba	$\geq 2.2 \times 10^{21}$ [37]	≤ 3.335
Nucleus	$T_{1/2}^{2\nu\beta^-\beta^-}$ (yr)	$\left\|M_{\text{eff}}^{2\nu\beta^-\beta^-}\right\|$
^{134}Xe	$\geq 2.8 \times 10^{22}$ [66]	≤ 0.398

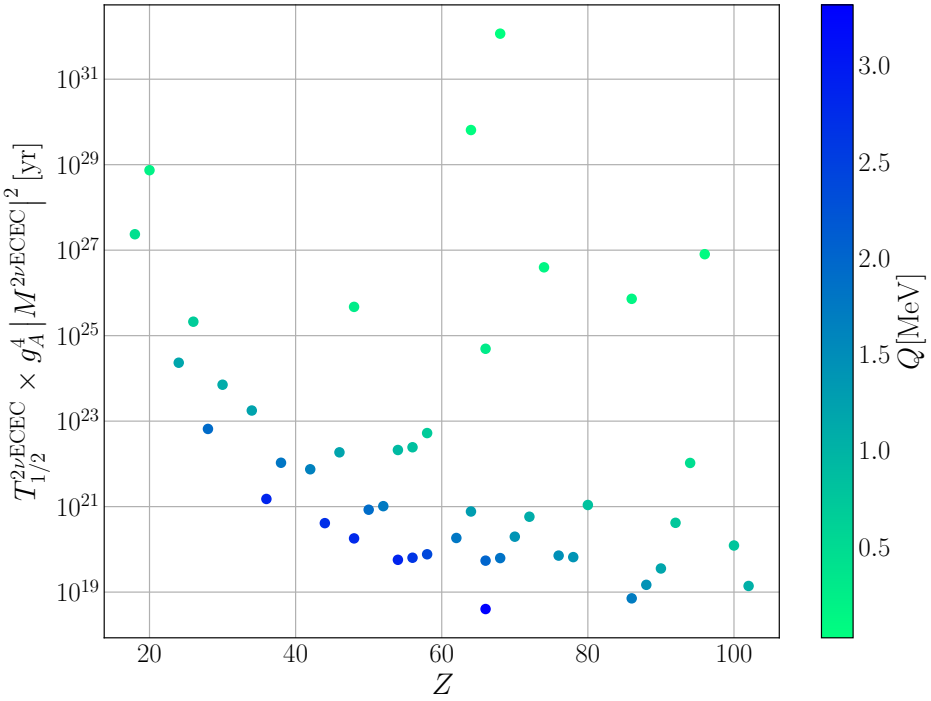

Figure 2. Theoretical half-life scaled by $g_A^4 \left| M^{2\nu\mathrm{ECEC}} \right|^2$ as function of atomic number for nuclei presented in Table 3. The color scale indicates the Q-value for each transition.

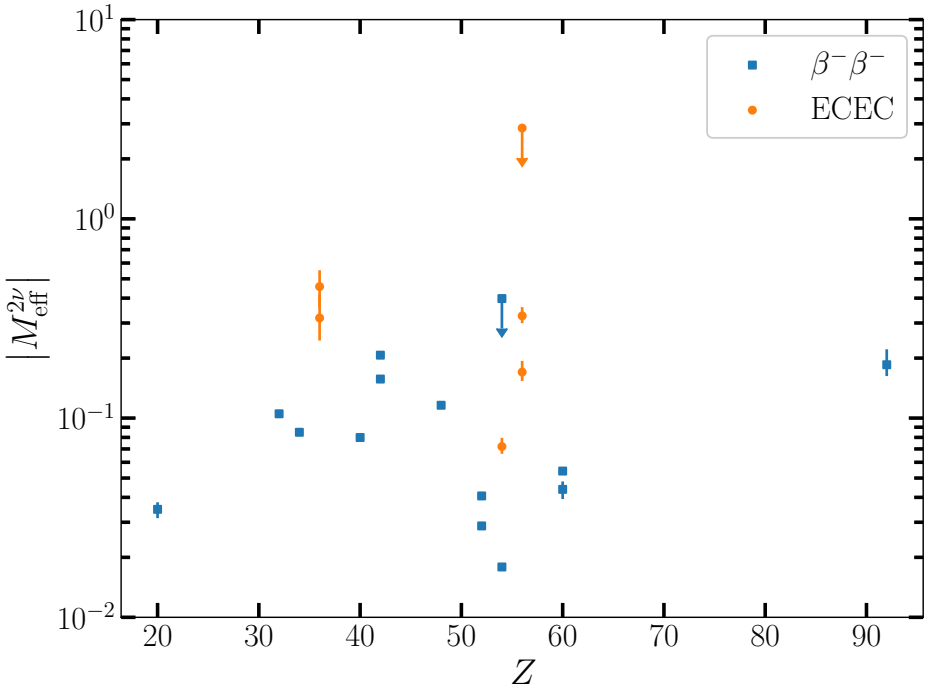

Figure 3. Absolute values of the effective nuclear matrix elements for the measured nuclei undergoing 2νECEC process or $2\nu\beta^-\beta^-$ decay. The values for 2νECEC processes and $2\nu\beta^-\beta^-$ decay of ^{134}Xe are the ones from Table 5. The other $2\nu\beta^-\beta^-$ values are the ones reported in [20], computed using the PSFs from [65]. Vertical bars indicate uncertainties derived from the ones of the measured half-lives. Arrows indicate that the corresponding point is an upper limit for the effective nuclear matrix element.

4. Uncertainties and Further Improvements

We first perform a sensitivity analysis on the input parameters, namely the Q-value, the average energy of the excited 1^+ states $\langle E_N \rangle$ and the nuclear radius. The relative variations in the PSFs due to each parameter are summarized in Table 6, with the Q-value having the highest influence. However, we note that modern determinations of this quantity are highly accurate and the absolute values of the PSFs are practically insensitive to the choice of Q-value. The sensitivity of the PSFs with respect to $\langle E_N \rangle$ and the nuclear radius are much smaller, as noted previously in [49].

Table 6. Summary of uncertainties in the PSFs due to input parameters.

Source	$\delta G^{2\nu\text{ECEC}}_{K\to\text{edge}}/G^{2\nu\text{ECEC}}_{K\to\text{edge}}$
Q-value	$(5\text{–}7)\times\delta Q/Q$
$\langle E_N \rangle$	$0.07\times\delta\langle E_N\rangle/\langle E_N\rangle$
Nuclear radius	$0.2\times\delta R/R$

Another source of uncertainties is related to the choice of the DHFS model for atomic structure computations. The accuracy of the binding energies obtained in the DHFS approach is around 1% relative to the experimental values [58]. The binding energies enter in the PSFs definition through the integration limit, through the energies of the emitted neutrinos, and through the $\langle K_N \rangle$ and $\langle L_N \rangle$ factors, always as additive quantities to the Q-value. Consequently, this uncertainty has a negligible effect as it translates to $\mathcal{O}(10^{-4})$ relative variation in the Q-value of the process. Low Q-value transitions are an exception, and the uncertainty in the binding energies is dominant. The values of the wave functions on the nuclear surface can also introduce some uncertainty in the PSFs. This effect was studied in [58] by comparing the Coulomb amplitudes (proportional to the wave function values on the nuclear surface) in the DHFS model with the ones obtained through more complex models. The study found that Coulomb amplitudes obtained in the DHFS framework agree within 0.25% with ones obtained through the more refined Dirac–Hartree–Fock (DHF) model for the $1s_{1/2}$ and $2s_{1/2}$ shells and for atomic numbers above 20. Considering this value as uncertainty within our model, we evaluate the relative error in the PSFs due to the wave functions alone to be 1%, since the wave functions enter the PSF definition to the fourth power. We note that this uncertainty is a systematic one, the Coulomb amplitudes in the DHFS model always overestimating the ones obtained in the DHF model.

Besides the uncertainties discussed above, one may expect variations in PSFs from improving the overall model of the 2νECEC process. Firstly, the summed neutrino energy determination has been obtained through a usual approximation (see Equation (6)), but it can be more precisely determined through Equation (5). Consequences are most important in low Q-value transitions. For example, the DHFS framework predicts $R_{KL_1} = 55.05$ keV for ^{152}Sm. Consequently, the $2\nu KL_1$ process of ^{152}Gd is energetically allowed (in contrast to the results shown in Table 3), as it was also found in [67–69] when studying the resonant neutrinoless double electron capture. Secondly, the Pauli blocking of the decay of the innermost nucleon states is not accounted for in our model. This aspect can be improved by averaging the bound electron wave function, weighted with a realistic nuclear charge distribution [65,70]. From preliminary results, we expect an increase of a few % in the PSFs due to the Pauli blocking effect.

5. Conclusions

In this paper, we have conducted a systematic study of atoms undergoing the 2νECEC process. Despite the fact that 2νECEC, by its very nature, resides at the interface between nuclear and atomic physics, certain aspects related to atomic structure calculations have been either overlooked or treated simplistically in previous investigations. In our model, we introduced two enhancements to the atomic part calculations of double electron capture

transitions. Firstly, by employing the DHFS self-consistent framework to describe the initial atomic system, we refined both the distortion of bound wave functions due to atomic clouds and the estimation of binding energies for captured electrons. Secondly, we extended our consideration beyond previous studies, where only K and L_1 orbitals were included, by also allowing captures from the outer orbitals of the initial atoms.

With our improved model, we have updated the phase-space values for all atoms undergoing the 2νECEC process. For light atoms, we observed almost no differences compared to a previous model, where a simplified atomic screening and only captures from K and L_1 orbitals were considered. This lack of difference is associated with a cancellation of the decrease in the decay rate from a more precise screening treatment with the increase associated with the possibility of captures occurring from higher orbitals. In contrast, for medium and heavy atoms, we observed an increase in the decay rate, almost linear in Z, reaching about 10% for the heaviest atoms. In the systematic study, we also provided capture fractions for the first few dominant partial channels and separately addressed the low Q-value 2νECEC transitions of ^{152}Gd, ^{164}Er, and ^{242}Cm, for which the KK capture is energetically forbidden. Finally, we demonstrated that the effective nuclear matrix elements for both 2νECEC processes and $2\nu\beta^-\beta^-$ decays span similar ranges.

Author Contributions: Conceptualization, O.N., S.G., S.S. and F.Š.; methodology, O.N. and S.G.; software, S.G.; validation, O.N., S.G., S.S. and F.Š.; formal analysis, S.S. and F.Š.; investigation, O.N. and S.G.; resources, S.S. and F.Š.; data curation, O.N. and S.G.; writing—original draft preparation, O.N. and S.G.; writing—review and editing, O.N., S.G., S.S. and F.Š.; visualization, O.N. and S.G.; supervision, S.S. and F.Š.; project administration, F.Š.; funding acquisition, S.S. and F.Š. All authors have read and agreed to the published version of the manuscript.

Funding: O.N., S.G. and S.S. acknowledge support from the Romanian Ministry of Research, Innovation, and Digitalization through Project No. PN 23 08 641 04 04/2023. F.Š. acknowledges support from the Slovak Research and Development Agency under Contract No. APVV-22-0413 and by the Czech Science Foundation (GAČR), project No. 24-10180S.

Data Availability Statement: The original contributions presented in the study are included in the article, further inquiries can be directed to the corresponding author.

Conflicts of Interest: The authors declare no conflicts of interest.

References

1. Majorana, E. Teoria simmetrica dell'elettrone e del positrone. *Il Nuovo C.* **1937**, *14*, 171–184. [CrossRef]
2. Schechter, J.; Valle, J.W.F. Neutrino decay and spontaneous violation of lepton number. *Phys. Rev. D* **1982**, *25*, 774–783. [CrossRef]
3. Sujkowski, Z.; Wycech, S. Neutrinoless double electron capture: A tool to search for Majorana neutrinos. *Phys. Rev. C* **2004**, *70*, 052501. [CrossRef]
4. Pascoli, S.; Petcov, S.; Schwetz, T. The absolute neutrino mass scale, neutrino mass spectrum, Majorana CP-violation and neutrinoless double-beta decay. *Nucl. Phys. B* **2006**, *734*, 24–49. [CrossRef]
5. Bilenky, S.M.; Giunti, C. Neutrinoless double-beta decay: A probe of physics beyond the Standard Model. *Int. J. Mod. Phys. A* **2015**, *30*, 1530001. [CrossRef]
6. Vergados, J.D.; Ejiri, H.; Šimkovic, F. Neutrinoless double beta decay and neutrino mass. *Int. J. Mod. Phys. E* **2016**, *25*, 1630007. [CrossRef]
7. Girardi, I.; Petcov, S.; Titov, A. Predictions for the Majorana CP violation phases in the neutrino mixing matrix and neutrinoless double beta decay. *Nucl. Phys. B* **2016**, *911*, 754–804. [CrossRef]
8. Šimkovic, F. Neutrino masses and interactions and neutrino experiments in the laboratory. *Physics-Uspekhi* **2021**, *64*, 1238. [CrossRef]
9. Fukugita, M.; Yanagida, T. Barygenesis without grand unification. *Phys. Lett. B* **1986**, *174*, 45–47. [CrossRef]
10. Buchmüller, W.; Peccei, R.; Yanagida, T. Leptogenesis as the origin of matter. *Annu. Rev. Nucl. Part. Sci.* **2005**, *55*, 311–355. [CrossRef]
11. Ebert, J.; Fritts, M.; Gehre, D.; Gößling, C.; Hagner, C.; Heidrich, N.; Klingenberg, R.; Kröninger, K.; Nitsch, C.; Oldorf, C.; et al. Results of a search for neutrinoless double-β decay using the COBRA demonstrator. *Phys. Rev. C* **2016**, *94*, 024603. [CrossRef]
12. Barabash, A.S.; Belli, P.; Bernabei, R.; Cappella, F.; Caracciolo, V.; Cerulli, R.; Chernyak, D.M.; Danevich, F.A.; d'Angelo, S.; Incicchitti, A.; et al. Final results of the Aurora experiment to study 2β decay of ^{116}Cd with enriched $^{116}CdWO_4$ crystal scintillators. *Phys. Rev. D* **2018**, *98*, 092007. [CrossRef]

13. Anton, G.; Badhrees, I.; Barbeau, P.S.; Beck, D.; Belov, V.; Bhatta, T.; Breidenbach, M.; Brunner, T.; Cao, G.F.; Cen, W.R.; et al. Search for Neutrinoless Double-β Decay with the Complete EXO-200 Dataset. *Phys. Rev. Lett.* **2019**, *123*, 161802. [CrossRef] [PubMed]
14. Agostini, M. et al. [GERDA Collaboration]. Final Results of GERDA on the Search for Neutrinoless Double-β Decay. *Phys. Rev. Lett.* **2020**, *125*, 252502. [CrossRef] [PubMed]
15. Azzolini, O.; Beeman, J.W.; Bellini, F.; Beretta, M.; Biassoni, M.; Brofferio, C.; Bucci, C.; Capelli, S.; Caracciolo, V.; Cardani, L.; et al. Final Result on the Neutrinoless Double Beta Decay of ^{82}Se with CUPID-0. *Phys. Rev. Lett.* **2022**, *129*, 111801. [CrossRef]
16. Adams, D.Q. et al. [CUORE Collaboration]. New Direct Limit on Neutrinoless Double Beta Decay Half-Life of ^{128}Te with CUORE. *Phys. Rev. Lett.* **2022**, *129*, 222501. [CrossRef] [PubMed]
17. Abe, S. et al. [KamLAND-Zen Collaboration]. Search for the Majorana Nature of Neutrinos in the Inverted Mass Ordering Region with KamLAND-Zen. *Phys. Rev. Lett.* **2023**, *130*, 051801. [CrossRef]
18. Arnquist, I.J. et al. [Majorana Collaboration]. Final Result of the Majorana Demonstrator's Search for Neutrinoless Double-β Decay in ^{76}Ge. *Phys. Rev. Lett.* **2023**, *130*, 062501. [CrossRef]
19. Saakyan, R. Two-Neutrino Double-Beta Decay. *Annu. Rev. Nucl. Part. Sci.* **2013**, *63*, 503–529. [CrossRef]
20. Barabash, A. Precise Half-Life Values for Two-Neutrino Double-β Decay: 2020 Review. *Universe* **2020**, *6*, 159. [CrossRef]
21. Barabash, A. Double Beta Decay Experiments: Recent Achievements and Future Prospects. *Universe* **2023**, *9*, 290. [CrossRef]
22. Deppisch, F.F.; Graf, L.; Rodejohann, W.; Xu, X.J. Neutrino self-interactions and double beta decay. *Phys. Rev. D* **2020**, *102*, 051701. [CrossRef]
23. Deppisch, F.F.; Graf, L.; Šimkovic, F. Searching for New Physics in Two-Neutrino Double Beta Decay. *Phys. Rev. Lett.* **2020**, *125*, 171801. [CrossRef]
24. Barabash, A.; Dolgov, A.; Dvornický, R.; Šimkovic, F.; Smirnov, A. Statistics of neutrinos and the double beta decay. *Nucl. Phys. B* **2007**, *783*, 90–111. [CrossRef]
25. Bolton, P.D.; Deppisch, F.F.; Gráf, L.; Šimkovic, F. Two-neutrino double beta decay with sterile neutrinos. *Phys. Rev. D* **2021**, *103*, 055019. [CrossRef]
26. Agostini, M.; Bossio, E.; Ibarra, A.; Marcano, X. Search for light exotic fermions in double-beta decays. *Phys. Lett. B* **2021**, *815*, 136127. [CrossRef]
27. Díaz, J.S. Limits on Lorentz and *CPT* violation from double beta decay. *Phys. Rev. D* **2014**, *89*, 036002. [CrossRef]
28. Nițescu, O.; Ghinescu, S.; Stoica, S. Lorentz violation effects in $2\nu\beta\beta$ decay. *J. Phys. G Nucl. Part. Phys.* **2020**, *47*, 055112. [CrossRef]
29. Ghinescu, S.A.; Nițescu, O.; Stoica, S. Investigation of the Lorentz invariance violation in two-neutrino double-beta decay. *Phys. Rev. D* **2022**, *105*, 055032. [CrossRef]
30. Arnold, R. et al. [NEMO Collaboration]. Limits on different majoron decay modes of 100Mo and 82Se for neutrinoless double beta decays in the NEMO-3 experiment. *Nucl. Phys. A* **2006**, *765*, 483–494. [CrossRef]
31. Arnold, R.; Augier, C.; Barabash, A.S.; Basharina-Freshville, A.; Blondel, S.; Blot, S.; Bongrand, M.; Boursette, D.; Brudanin, V.; Busto, J.; et al. Detailed studies of ^{100}Mo two-neutrino double beta decay in NEMO-3. *Eur. Phys. J. C* **2019**, *79*, 440. [CrossRef]
32. Arnold, R. et al. [NEMO-3 Collaboration]. Search for Neutrinoless Quadruple-β Decay of ^{150}Nd with the NEMO-3 Detector. *Phys. Rev. Lett.* **2017**, *119*, 041801. [CrossRef] [PubMed]
33. Bossio, E.; Agostini, M. Probing beyond the standard model physics with double-beta decays. *J. Phys. G Nucl. Part. Phys.* **2023**, *51*, 023001. [CrossRef]
34. Belli, P.; Bernabei, R.; Caracciolo, V. Status and Perspectives of 2ϵ, $\epsilon\beta+$ and 2β Decays. *Particles* **2021**, *4*, 241–274. [CrossRef]
35. Doi, M.; Kotani, T. Neutrino Emitting Modes of Double Beta Decay. *Prog. Theor. Phys.* **1992**, *87*, 1207–1231. [CrossRef]
36. Doi, M.; Kotani, T. Neutrinoless Modes of Double Beta Decay. *Prog. Theor. Phys.* **1993**, *89*, 139–159. [CrossRef]
37. Barabash, A.S.; Saakyan, R.R. Experimental limits on $2\beta^+$, Kβ^+, and 2K processes for ^{130}Ba and on 2K capture for ^{132}Ba. *Phys. At. Nucl.* **1996**, *59*, 179–184.
38. Meshik, A.P.; Hohenberg, C.M.; Pravdivtseva, O.V.; Kapusta, Y.S. Weak decay of ^{130}Ba and ^{132}Ba: Geochemical measurements. *Phys. Rev. C* **2001**, *64*, 035205. [CrossRef]
39. Pujol, M.; Marty, B.; Burnard, P.; Philippot, P. Xenon in Archean barite: Weak decay of 130Ba, mass-dependent isotopic fractionation and implication for barite formation. *Geochim. Cosmochim. Acta* **2009**, *73*, 6834–6846. [CrossRef]
40. Gavrilyuk, Y.M.; Gangapshev, A.M.; Kazalov, V.V.; Kuzminov, V.V.; Panasenko, S.I.; Ratkevich, S.S. Indications of $2\nu2K$ capture in ^{78}Kr. *Phys. Rev. C* **2013**, *87*, 035501. [CrossRef]
41. Ratkevich, S.S.; Gangapshev, A.M.; Gavrilyuk, Y.M.; Karpeshin, F.F.; Kazalov, V.V.; Kuzminov, V.V.; Panasenko, S.I.; Trzhaskovskaya, M.B.; Yakimenko, S.P. Comparative study of the double-*K*-shell-vacancy production in single- and double-electron-capture decay. *Phys. Rev. C* **2017**, *96*, 065502. [CrossRef]
42. Aprile, E. et al. [XENON Collaboration]. Observation of two-neutrino double electron capture in 124Xe with XENON1T. *Nature* **2019**, *568*, 532–535. [CrossRef] [PubMed]
43. Aprile, E. et al. [XENON Collaboration]. Double-weak decays of ^{124}Xe and ^{136}Xe in the XENON1T and XENONnT experiments. *Phys. Rev. C* **2022**, *106*, 024328. [CrossRef]
44. Primakoff, H.; Rosen, S.P. Double beta decay. *Rep. Prog. Phys.* **1959**, *22*, 121. [CrossRef]
45. Primakoff, H.; Rosen, S.P. A Corrigendum to the Article 'Double Beta Decay' by H. Primakoff and S. P. Rosen in Reports on Progress in Physics. *Proc. Phys. Soc.* **1961**, *78*, 464. [CrossRef]

46. Vergados, J. Lepton-violating $\beta^-\beta^-$, $\beta^+\beta^+$ decays, (e^-, e^+) conversion and double electron capture in gauge theories. *Nucl. Phys. B* **1983**, *218*, 109–144. [CrossRef]
47. Kim, C.W.; Kubodera, K. Double-positron decay, positron-emitting *K* capture, and double *K* capture. *Phys. Rev. D* **1983**, *27*, 2765–2768. [CrossRef]
48. Boehm, F.; Vogel, P. *Physics of Massive Neutrinos*; Cambridge University Press: Cambridge, UK, 1992.
49. Kotila, J.; Iachello, F. Phase space factors for $\beta^+\beta^+$ decay and competing modes of double-β decay. *Phys. Rev. C* **2013**, *87*, 024313. [CrossRef]
50. Mirea, M.; Pahomi, T.; Stoica, S. Values of the phase space factors involved in double beta decay. *Rom. Rep. Phys.* **2015**, *67*, 872–889.
51. Stoica, S.; Mirea, M. Phase Space Factors for Double-Beta Decays. *Front. Phys.* **2019**, *7*, 12. [CrossRef]
52. Martínez-Lema, G. et al. [NEXT Collaboration]. Sensitivity of the NEXT experiment to Xe-124 double electron capture. *J. High Energy Phys.* **2021**, *2021*, 1029–8479. [CrossRef]
53. Haxton, W.; Stephenson, G. Double beta decay. *Prog. Part. Nucl. Phys.* **1984**, *12*, 409–479. [CrossRef]
54. Suhonen, J. Double beta decays of 124Xe investigated in the QRPA framework. *J. Phys. G Nucl. Part. Phys.* **2013**, *40*, 075102. [CrossRef]
55. Pirinen, P.; Suhonen, J. Systematic approach to β and $2\nu\beta\beta$ decays of mass $A = 100 - 136$ nuclei. *Phys. Rev. C* **2015**, *91*, 054309. [CrossRef]
56. Coello Pérez, E.; Menéndez, J.; Schwenk, A. Two-neutrino double electron capture on 124Xe based on an effective theory and the nuclear shell model. *Phys. Lett. B* **2019**, *797*, 134885. [CrossRef]
57. Niţescu, O.; Stoica, S.; Šimkovic, F. Exchange correction for allowed β decay. *Phys. Rev. C* **2023**, *107*, 025501. [CrossRef]
58. Sevestrean, V.A.; Niţescu, O.; Ghinescu, S.; Stoica, S. Self-consistent calculations for atomic electron capture. *Phys. Rev. A* **2023**, *108*, 012810. [CrossRef]
59. Salvat, F.; Fernández-Varea, J.M. RADIAL: A Fortran subroutine package for the solution of the radial Schrödinger and Dirac wave equations. *Comput. Phys. Commun.* **2019**, *240*, 165–177. [CrossRef]
60. Lotz, W. Electron Binding Energies in Free Atoms*. *J. Opt. Soc. Am.* **1970**, *60*, 206–210. [CrossRef]
61. Wang, M.; Huang, W.; Kondev, F.; Audi, G.; Naimi, S. The AME 2020 atomic mass evaluation (II). Tables, graphs and references*. *Chin. Phys. C* **2021**, *45*, 030003. [CrossRef]
62. Barabash, A.S. Does the weak interaction constant depend on time? *J. Exp. Theor. Phys. Lett.* **1998**, *68*, 1–6. [CrossRef]
63. Barabash, A.S. Possible evidence for a time variation of the weak-interaction constant from double-beta-decay experiments. *Phys. At. Nucl.* **2000**, *63*, 1210–1213. [CrossRef]
64. Barabash, A.S. Possible Evidence of Time Variation of Weak Interaction Constant from Double Beta Decay Experiments. *Astrophys. Space Sci.* **2003**, *283*, 607–612. [CrossRef]
65. Kotila, J.; Iachello, F. Phase-space factors for double-β decay. *Phys. Rev. C* **2012**, *85*, 034316. [CrossRef]
66. Yan, X.; Cheng, Z.; Abdukerim, A.; Bo, Z.; Chen, W.; Chen, X.; Cheng, C.; Cui, X.; Fan, Y.; Fang, D.; et al. Searching for Two-Neutrino and Neutrinoless Double Beta Decay of ^{134}Xe with the PandaX-4T Experiment. *arXiv* **2023**, arXiv:2312.15632.
67. Eliseev, S.; Roux, C.; Blaum, K.; Block, M.; Droese, C.; Herfurth, F.; Kluge, H.J.; Krivoruchenko, M.I.; Novikov, Y.N.; Minaya Ramirez, E.; et al. Resonant Enhancement of Neutrinoless Double-Electron Capture in ^{152}Gd. *Phys. Rev. Lett.* **2011**, *106*, 052504. [CrossRef] [PubMed]
68. Krivoruchenko, M.; Šimkovic, F.; Frekers, D.; Faessler, A. Resonance enhancement of neutrinoless double electron capture. *Nucl. Phys. A* **2011**, *859*, 140–171. [CrossRef]
69. Blaum, K.; Eliseev, S.; Danevich, F.A.; Tretyak, V.I.; Kovalenko, S.; Krivoruchenko, M.I.; Novikov, Y.N.; Suhonen, J. Neutrinoless double-electron capture. *Rev. Mod. Phys.* **2020**, *92*, 045007. [CrossRef]
70. Šimkovic, F.; Dvornický, R.; Vogel, P. Muon capture rates: Evaluation within the quasiparticle random phase approximation. *Phys. Rev. C* **2020**, *102*, 034301. [CrossRef]